Monthly Notices
of the
ROYAL ASTRONOMICAL SOCIETY

MNRAS **450,** 3829–3839 (2015) doi:10.1093/mnras/stv933

Intensity mapping of [C II] emission from early galaxies

B. Yue,[1⋆] A. Ferrara,[1,2] A. Pallottini,[1] S. Gallerani[1] and L. Vallini[1,3]

[1]*Scuola Normale Superiore, Piazza dei Cavalieri 7, I-56126 Pisa, Italy*
[2]*Kavli IPMU (WPI), Todai Institutes for Advanced Study, the University of Tokyo, 5-1-5 Kashiwanoha, Kashiwa 277-8583, Japan*
[3]*Dipartimento di Fisica e Astronomia, Universitá di Bologna, viale Berti Pichat 6/2, I-40127 Bologna, Italy*

Accepted 2015 April 23. Received 2015 April 20; in original form 2015 February 4

ABSTRACT

The intensity mapping of the [C II] 157.7-μm fine-structure emission line represents an ideal experiment to probe star formation activity in galaxies, especially in those that are too faint to be individually detected. Here, we investigate the feasibility of such an experiment for $z > 5$ galaxies. We construct the $L_{\rm C\,II}-M_{\rm h}$ relation from observations and simulations, then generate mock [C II] intensity maps by applying this relation to halo catalogues built from large scale *N*-body simulations. Maps of the extragalactic far-infrared (FIR) continuum, referred to as 'foreground', and CO rotational transition lines and [C I] fine-structure lines referred to as 'contamination', are produced as well. We find that, at 316 GHz (corresponding to $z_{\rm C\,II} = 5$), the mean intensities of the extragalactic FIR continuum, [C II] signal, all CO lines from $J = 1$ to 13 and two [C I] lines are $\sim 3 \times 10^5$, $\sim$1200, $\sim$800, and $\sim$100 Jy sr^{-1}, respectively. We discuss a method that allows us to subtract the FIR continuum foreground by removing a spectrally smooth component from each line of sight, and to suppress the CO/[C I] contamination by discarding pixels that are bright in contamination emission. The $z > 5$ [C II] signal comes mainly from haloes in the mass range $10^{11-12}\,{\rm M}_\odot$; as this mass range is narrow, intensity mapping is an ideal experiment to investigate these early galaxies. In principle such signal is accessible to a ground-based telescope with a 6 m aperture, 150-K system temperature, a 128 × 128 pixels FIR camera in 5000-h total integration time; however, it is difficult to perform such an experiment by using currently available telescopes.

Key words: galaxies: high-redshift – dark ages, reionization, first stars – diffuse radiation – radio lines: galaxies.

1 INTRODUCTION

The emission line intensity mapping is a technique to access high-z galaxies below the detection limit without losing redshift information, as proposed by e.g. Visbal & Loeb (2010), Visbal, Trac & Loeb (2011), Gong et al. (2011), Gong et al. (2012), Gong, Cooray & Santos (2013), Lidz et al. (2011), Silva et al. (2013), and Pullen, Doré & Bock (2014). Optimistically, it only collects radiation from galaxies in a selected redshift range, as the spurious flux due to foregrounds, contaminating radiation and noise can be in principle removed or suppressed. Compared with galaxy surveys that aim at resolving faint spots in a limited field of view (FOV), the advantages of intensity mapping rely on the fact that, if the galaxy luminosity function (LF) has a sufficiently steep faint end, the observed radiation is actually dominated by unresolved sources (Uzgil et al. 2014). Even if this is not the case, intensity mapping can still be used to study unresolved galaxies once resolved sources are removed (masked). Interestingly, an intensity mapping experiment could be carried out with a modest aperture but large FOV telescope.

The [C II] 157.7-μm fine-structure line arising from the $^2{\rm P}_{3/2}\rightarrow{}^2{\rm P}_{1/2}$ transition is the brightest amongst all metal lines emitted by the interstellar medium (ISM) of star-forming galaxies. It is associated to the star formation in galaxies (Boselli et al. 2002; de Looze et al. 2011; De Looze et al. 2014; Herrera-Camus et al. 2015) and plays a key role in the energy balance of galaxies, as it provides one of the most efficient cooling processes for the neutral ISM. With respect to the Ly α line, the [C II] line has the advantage of being unaffected by dust attenuation and neutral hydrogen absorption.

In the local Universe, [C II] line has been successfully detected even in galaxies with amazingly low star formation rates (SFR) of $\sim 0.001\,{\rm M}_\odot\ {\rm yr}^{-1}$ (De Looze et al. 2014). These authors have also derived the relation between the [C II] line luminosity, $L_{\rm C\,II}$, and the SFR of *local* galaxy samples (De Looze et al. 2014). Surprisingly, given the rather complicated physics behind the [C II] emission, $L_{\rm C\,II}$ scales rather tightly with SFR. However, at high redshift ($z \gtrsim 4$), the [C II] line has been detected so far only in quasar host galaxies (Maiolino et al. 2005; Gallerani et al. 2012;

⋆ E-mail: bin.yue@sns.it

Venemans et al. 2012; Wang et al. 2013; Willott, Omont & Bergeron 2013; Cicone et al. 2015) or ultraluminous infrared galaxies (ULIRGs, with $L_{\rm IR} > 10^{12} {\rm L}_{\odot}$ where $L_{\rm IR}$ is the in-band luminosity at 8-1000 μm) characterized by SFR $\sim 10^{2-3}$ $\mathrm{M}_{\odot}$ yr^{-1} (Cox et al. 2011; De Breuck et al. 2011, 2014). For typical normal star-forming galaxies (SFR $\sim 10\,\mathrm{M}_{\odot}\mathrm{yr}^{-1}$), [C II] emission has not yet been detected (Ouchi et al. 2013; González-López et al. 2014; Ota et al. 2014; Schaerer et al. 2015). This might indicate that most of carbon in these galaxies is at higher ionization state and/or their ISM is characterized by a very low level of metal enrichment. By applying the $L_{\rm C\,II}$–SFR relation derived from local galaxies samples to high-redshift Ly α emitters it is possible to compute the expected [C II] flux from these galaxies. The fact that their [C II] line remains undetected even with ALMA provides useful constraints on their internal radiation field, molecular content, gas density, and metallicity (Vallini et al. 2013, 2015; González-López et al. 2014).

As probing tools, intensity mapping experiments are affected by the presence of foreground radiation, including that represented by the galaxy continuum redshifted into the observed band. Unfortunately, it is almost often the case that the foreground intensity largely exceeds that of the signal. The typical [C II] line luminosity is 0.1–1 per cent of the $L_{\rm IR}$ (Maiolino et al. 2009). This implies that even if only one per cent of the IR luminosity is redshifted into the observed band, the continuum emission overcomes the [C II] line.

In addition to the far-infrared (FIR) continuum foreground, there are other emission lines emitted from a range of redshifts that fall at the same frequency of the [C II] signal; they act as *contaminants*. For example, the [O I] line with wavelength 145 μm, the two [N II] lines ($\lambda = 122, 205$ μm) and two [C I] lines ($\lambda = 610, 371$ μm), and a handful of CO rotational transition lines in the range 200–2610 μm. Among these, the CO rotational transition lines are the most relevant here. For example, since the CO(4–3) line has a wavelength 651 μm, if emitted from $z = 0.45$ galaxies, it contaminates the [C II] emission from $z = 5$ galaxies. The emission efficiency[1] of the CO(4–3) line from star-forming galaxies is ∼2 per cent of the [C II] line (Visbal & Loeb 2010). However, the luminosity distance from $z = 0$ to 0.45 is only ∼5 per cent of that to $z = 5$. As the flux is inversely proportional to the square of the luminosity distance, whereas the proper distance interval that corresponds to the same bandwidth is $\propto (1+z)^{-3/2}$, the CO flux can be more than 10 times higher than the [C II] one, even ignoring the cosmological evolution of the SFR density. Thus, CO contamination, as well as the continuum foreground, cannot be ignored and must be considered thoroughly.

Although the [C II] signal itself can be computed analytically (Gong et al. 2012; Uzgil et al. 2014), a reliable investigation of the influence of foreground/contamination is only possible based on mock maps that carefully mimic observations as close as possible. This is the prime motivation of this paper. Using halo catalogues recovered from large scale *N*-body simulations, we produce mock maps including (a) [C II] signal, (b) FIR continuum foreground, (c) CO and [C I] contamination lines, and (d) instrumental noise. We then test our foreground/contamination removal scheme on these maps to demonstrate the successful recovery of the original [C II] signal.

The layout of this paper is as follows. In Section 2, we describe the model used to compute the [C II] from high-z galaxies and the necessary steps to generate mock maps. We show our forecasts for the [C II] signal, extragalactic FIR continuum and the contamination and perform foreground/contamination removal experiments on mocks to recover the original [C II] signal. The results are presented in Section 3. The conclusions and discussion are found in Section 4.

2 METHODS

2.1 [C II] emission from early galaxies

Vallini et al. (2013) and Vallini et al. (2015, hereafter V15) have combined high-z galaxy numerical simulations with subgrid models of the ISM to compute the expected [C II] luminosity ($L_{\rm C\,II}$) arising from diffuse neutral gas and photodissociation regions (PDRs). The resulting trend of $L_{\rm C\,II}$ with SFR and metallicity (Z) is consistent with observations of local metal-poor dwarf galaxies (De Looze et al. 2014). For the range [0.1,100] $\mathrm{M}_{\odot}$ yr^{-1} and [0.05,1.0] $\mathrm{Z}_{\odot}$ which should encompass most of the sources contributing to the total [C II] emission at high redshift, V15 results are well reproduced by the following fitting formula:

$$\log(L_{\rm C\,II}) = 7.0 + 1.2 \times \log({\rm SFR}) + 0.021 \times \log(Z) + 0.012 \times \log({\rm SFR})\log(Z) - 0.74 \times \log^2(Z), \quad (1)$$

where $L_{\rm C\,II}$, SFR, and Z are in units of $\mathrm{L}_{\odot}$, $\mathrm{M}_{\odot}$ yr^{-1}, and $\mathrm{Z}_{\odot}$, respectively.

The next step is to compute the $L_{\rm C\,II}$–$M_{\rm h}$ relation, where $M_{\rm h}$ is the halo mass. To this aim we need to know the SFR–$M_{\rm h}$ and Z–$M_{\rm h}$ relations. We obtain them from the procedure described in below paragraphs.[2]

Since the UV luminosity ($L_{\rm UV}$) of a galaxy scales with its SFR (e.g. Kennicutt 1998), we adopt the observed UV LFs to derive the SFR–$M_{\rm h}$ relation. The *measured* UV LF is well described by a Schechter parametrization (Schechter 1976):

$$\frac{{\rm d}n}{{\rm d}M_{\rm UV}} = 0.4\ln(10)\,\phi_\star\, x^{1+\alpha} {\rm e}^{-x}, \quad (2)$$

where $x = 10^{0.4(M^\star_{\rm UV} - M_{\rm UV})}$, with $M_{\rm UV}$ the dust-attenuated absolute magnitude. For the rest-frame UV luminosity at 1600 Å, the redshift-dependent parameters ($M^\star_{\rm UV}, \phi_\star, \alpha$) that fit observations between $z \sim 4$–8 are (Bouwens et al. 2015)

$$\begin{aligned} M^\star_{\rm UV} &= -20.96 + 0.01(z-6) \\ \phi_\star &= 0.46 \times 10^{-0.27(z-6)} 10^{-3} \\ \alpha &= -1.87 - 0.10(z-6). \end{aligned} \quad (3)$$

The intrinsic absolute magnitude is $M'_{\rm UV} = M_{\rm UV} - A_{1600}$, where $A_{1600} = 4.43 + 1.99\beta\ (\geq 0)$ is the dust attenuation at 1600 Å (Meurer, Heckman & Calzetti 1999) and β is the measured spectral slope ($f_\lambda \propto \lambda^\beta$). Normally β depends on $M_{\rm UV}$ and is fitted by (Bouwens et al. 2014)

$$\beta = \beta_{-19.5} + \frac{{\rm d}\beta}{{\rm d}M_{\rm UV}}(M_{\rm UV} + 19.5). \quad (4)$$

From fig. 2 of Bouwens et al. (2014) we find the following redshift-dependent fit, valid for $4 \lesssim z \lesssim 7$:

$$\begin{aligned} \beta_{-19.5} &= -1.97 - 0.06(z-6) \\ \frac{{\rm d}\beta}{{\rm d}M_{\rm UV}} &= -0.18 - 0.03(z-6). \end{aligned} \quad (5)$$

[1] As a caveat, we note that there is no clear consensus in the literature on this value; see Breysse, Kovetz & Kamionkowski (2014).

[2] Note that, compared to galaxies, the intergalactic medium emits a negligible [C II] signal (e.g. Gong et al. 2012) at $z \gtrsim 2$, and therefore is not considered in this work.

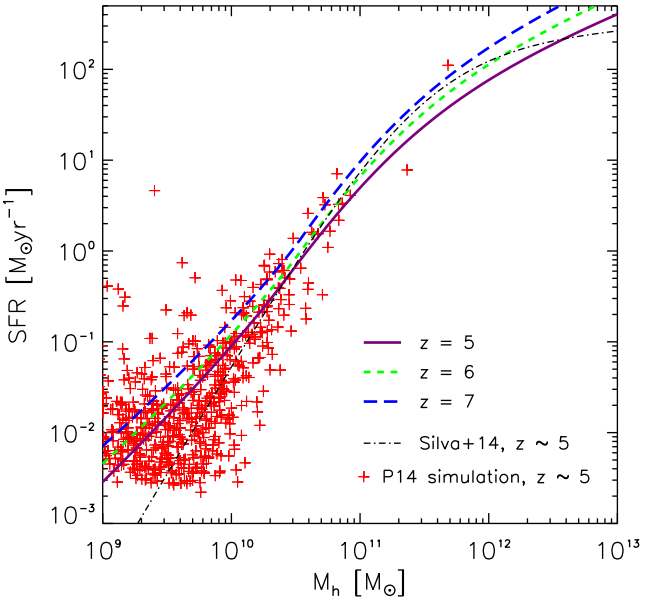

Figure 1. The SFR derived from UV LFs as a function of halo mass at $z = 5, 6,$ and 7, respectively. The SFR–$M_{\rm h}$ relation in Silva et al. (2014) at $z \sim 5$ and the SFR of each halo containing Pop II stars in P14 simulation at $z \sim 5$ are also shown.

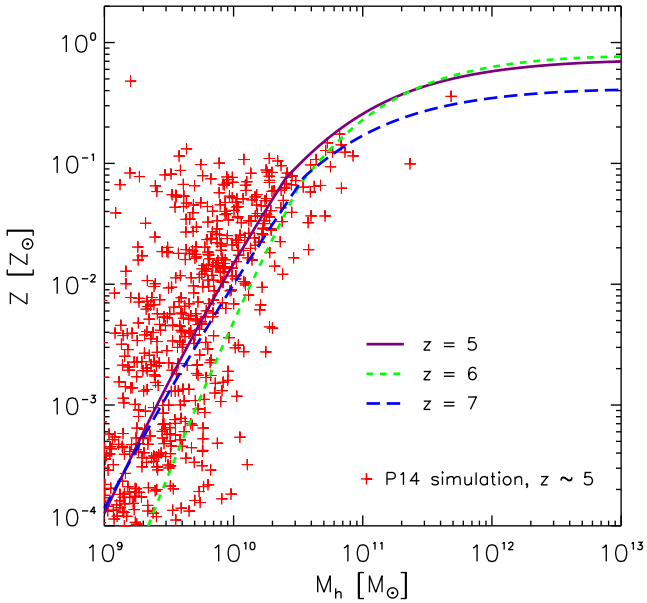

Figure 2. Metallicity, derived from mass-to-light ratio and the FMR, as a function of halo mass at $z = 5, 6,$ and 7. The metallicity of each halo containing Pop II stars in the P14 simulation at $z \sim 5$ are also shown.

The intrinsic UV LF is then connected to the measured UV LF via

$$\frac{{\rm d}n'}{{\rm d}M'_{\rm UV}}(M'_{\rm UV}, z) = \frac{{\rm d}n}{{\rm d}M_{\rm UV}}(M_{\rm UV}, z). \quad (6)$$

Assuming that the intrinsic $L'_{\rm UV}$ monotonically increases with $M_{\rm h}$ and that all haloes host some star formation activity, we obtain the $L'_{\rm UV}-M_{\rm h}$ relation from

$$\int_{M'_{\rm UV}} \frac{{\rm d}n'}{{\rm d}M'_{\rm UV}}{\rm d}M'_{\rm UV} = \int_{M_{\rm h}} \frac{{\rm d}n}{{\rm d}M_{\rm h}}{\rm d}M_{\rm h}, \quad (7)$$

where ${\rm d}n/{\rm d}M_{\rm h}$ is the halo mass function (Sheth & Tormen 1999; Sheth, Mo & Tormen 2001). This 'abundance matching' technique will be used also in Section 2.2 to derive the relation between the IR luminosity and halo mass. We then derive the SFR from $L'_{\rm UV}$. In principle $L'_{\rm UV}$ depends not only on the SFR, but also on metallicity and stellar age. However, we note that the UV luminosity is insensitive to the metallicity and the stellar age, unless stars are very young ($\lesssim$10 Myr). So we can safely assume that $L'_{\rm UV}$ scales with SFR as

$$L'_{\rm UV} = l_{\rm UV} \times {\rm SFR}. \quad (8)$$

We compute $l_{\rm UV}$ from STARBURST99[3] (Leitherer et al. 1999; Vázquez & Leitherer 2005; Leitherer et al. 2010) by assuming a metallicity 0.1 $Z_\odot$, stellar age 10 per cent of Hubble time, and a Salpeter initial mass function between 0.1–100 $M_\odot$. We choose the 'continuous star formation' mode. At 1600 Å, $l_{\rm UV} = (8.9, 8.6, 8.3) \times 10^{27}$ erg s^{-1} Hz^{-1}($M_\odot$ yr^{-1})$^{-1}$ at $z = (5, 6, 7)$, which is similar to Kennicutt (1998).

We plot the SFR derived with this procedure at various redshifts as a function of $M_{\rm h}$ in Fig. 1. As a comparison we also plot the SFR–$M_{\rm h}$ relation at $z \sim 5$ found by Silva et al. (2014) who fit the relation using semi-analytical models of galaxy formation. As can be seen by inspecting this figure, the specific SFR, i.e. the SFR per unit mass, starts to drop at a turnover mass $\sim 10^{11}$ $M_\odot$. This is consistent with semi-analytical model predictions.

The final ingredient of equation (1) is Z. As the metallicity of high-z galaxies is very poorly constrained at present, we derive it by combining the $L'_{\rm UV}-M_{\rm h}$ relation with the 'fundamental metallicity relation' (FMR) that relates Z to the stellar Mass ($M_\star$) and SFR. The FMR inferred from low-z galaxy observations (Mannucci et al. 2010) is given by the following equation:

$$\begin{aligned}\log(Z) = {} & 0.21 + 0.37\log(M_{10}) - 0.14\log({\rm SFR}) \\ & - 0.19\log^2(M_{10}) - 0.054\log^2({\rm SFR}) \\ & + 0.12\log(M_{10})\log({\rm SFR}), \end{aligned} \quad (9)$$

where $M_{10} = M_\star/10^{10}$, $M_\star$ and Z are expressed in Solar units. No redshift evolution is found at least up to $z = 2.5$ (Mannucci et al. 2010); therefore we apply it also to high-z galaxies, with the caveat that deviations might appear for high-z galaxies. The stellar mass, $M_\star$, is linked to the UV absolute magnitude via the mass-to-light ratio. From the latest measurements (Duncan et al. 2014),

$$\log(M_\star) = \log(M^0_\star) + \frac{{\rm d}M_\star}{{\rm d}M_{\rm UV}}(M_{\rm UV} + 19.5), \quad (10)$$

where $\log(M^0_\star) = (9.00, 8.84, 8.63)$ and ${\rm d}M_\star/{\rm d}M_{\rm UV} = (-0.46, -0.54, -0.45)$ in the redshift ranges $4.5 \le z < 5.5$, $5.5 \le z < 6.5$, and $6.5 \le z < 7.5$, respectively, for the model without nebular line contribution. We use the observed UV magnitude $M_{\rm UV}$ (i.e. without dust correction), and we ignore the negligible difference between the UV luminosity at 1500 and 1600 Å. Fig. 2 shows the derived Z–$M_{\rm h}$ relation at $z = 5, 6,$ and 7.

We finally compute the [C II] luminosity of haloes with mass $M_{\rm h}$ by substituting the SFR and Z derived above into equation (1). Although different star formation histories may cause a scatter in the [C II] luminosities for haloes of a given mass, we neglect this effect because it only results in noise as long as the luminosity dispersion is independent of position on large scales. The $L_{\rm C\,II}-M_{\rm h}$ relation derived with the above procedure is shown in Fig. 3 by solid, short dashed and long dashed lines for $z = 5, 6,$ and 7, respectively.

[3] http://www.stsci.edu/science/starburst99/docs/default.htm

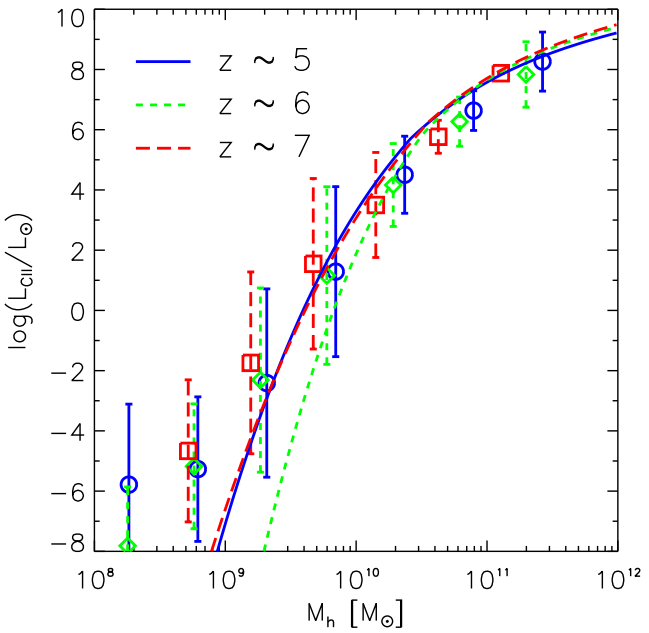

Figure 3. The mean $L_{\rm C\,II}$ as a function of halo mass, $M_{\rm h}$, at redshifts ∼5, 6, and 7, respectively. The lines are the relation derived using observations while the points are for the P14 simulation (the error bars are the standard deviation of $\langle\log(L_{\rm C\,II})\rangle$ for each mass bin).

When deriving the above $L_{\rm C\,II}-M_{\rm h}$ relation, the properties of faint galaxies are extrapolated from the observed bright galaxies. We check the validity of this relation by comparing the result obtained through this semi-empirical method with the numerical simulations of cosmic metal enrichment presented by Pallottini et al. (2014, hereafter P14). P14 have used a hydrodynamical simulation to follow the star formation and the Pop III–Pop II transition ($Z > 10^{-4}\,{\rm Z}_\odot$). Hereafter, we only consider the Pop II star formation mode.

If a halo has formed stars, it contains a number of stellar particles whose birth date and metallicity is recorded. For a selected halo, the mean stellar age is

$$t_{\rm age} = \frac{\sum_i \Delta t_i m_{\star,i}}{\sum_i m_{\star,i}}, \tag{11}$$

where Δt_i is the birth date of the ith stellar particle, $m_{\star,i}$ is its mass, and the sum is extended over all Pop II stellar particles in that halo. The mean metallicity of the halo is

$$Z = \frac{\sum_i Z_i m_{\star,i}}{\sum_i m_{\star,i}}, \tag{12}$$

where Z_i is the metallicity of the ith Pop II stellar particle. By dividing the total Pop II stellar mass by the mean age, we obtain the mean SFR of the halo,

$${\rm SFR} = \frac{\sum_i m_{\star,i}}{t_{\rm age}}. \tag{13}$$

The SFR versus $M_{\rm h}$ and Z versus $M_{\rm h}$ at $z \sim 5$ in P14 simulation are also plotted in Fig. 1 and Fig. 2, respectively.

Using equation (1) we calculate the [C II] luminosity of haloes from their SFR and Z and group haloes into several mass bins at each simulation output. Some haloes only have Pop III stars, or are too small to host any star formation. Therefore in each mass bin only a fraction $f_{\rm C\,II}$ of haloes exhibit [C II] emission. This fraction tends to one as the halo mass increases. We denote the mean log of [C II] luminosity for *haloes that exhibit [C II] emission* by $\langle\log(L_{\rm C\,II})\rangle$, and use

$$\log(L_{\rm C\,II}) = \langle\log(L_{\rm C\,II})\rangle + \log(f_{\rm C\,II}) \tag{14}$$

as the mean [C II] luminosity of *all* haloes with mass $M_{\rm h}$; this quantity is plotted in Fig. 3.

2.2 Far-infrared continuum foreground

In this subsection, we model the extragalactic foreground due to the FIR continuum from galaxies at different redshifts. The Milky Way FIR and cosmic microwave background (CMB) radiation are assumed to be removed straightforwardly and hence are not considered in this work.

The FIR LF of galaxies, including spiral galaxies, starburst galaxies, star-forming galaxies containing AGNs, and sometimes AGNs, is studied in e.g. Magnelli et al. (2009), Gruppioni et al. (2013), and Magnelli et al. (2013). In Gruppioni et al. (2013), the LF can be written as

$$\Phi = \Phi_\star \left(\frac{L_{\rm IR}}{L^\star_{\rm IR}}\right)^{1-\alpha} \exp\left[-\frac{1}{2\sigma^2}\log^2\left(1+\frac{L_{\rm IR}}{L^\star_{\rm IR}}\right)\right], \tag{15}$$

where $L_{\rm IR}$ is the infrared luminosity between 8-1000 μm. We use redshift evolution formulae of parameters $\alpha, \sigma, \Phi_\star, L^\star_{\rm IR}$ (Gruppioni et al. 2013): $\Phi_\star = 5.7\times10^{-3}(1+z)^{-0.57}$ for $z \le 1.1$, and $\Phi_\star = 6.81\times10^{-2}(1+z)^{-3.92}$ for $z > 1.1$; $L^\star_{\rm IR} = 7.68\times10^9(1+z)^{3.55}$ for $z \le 1.85$ and $L^\star_{\rm IR} = 5.80\times10^{10}(1+z)^{1.62}$ for $z > 1.85$; $\alpha = 1.15, \sigma = 0.52$ for $z \le 0.3$, and $\alpha = 1.2, \sigma = 0.5$ otherwise. The above LFs are constructed from galaxy samples at $z \lesssim 4.2$, therefore including the large majority of the sources contributing to the FIR continuum (and CO, which is associated to the FIR continuum; see next subsection).

We use again the abundance matching technique (Béthermin, Doré & Lagache 2012) to construct the $L_{\rm IR}$–$M_{\rm h}$ relation. We suppose that the contribution of subhaloes to the IR LF is small and we ignore them. By equating the number density of galaxies with IR luminosity above $L_{\rm IR}$ and the number density of haloes above $M_{\rm h}$,

$$\int_{L_{\rm IR}} \Phi(L_{\rm IR}, z){\rm d}L_{\rm IR} = \int_{M_{\rm h}} \frac{{\rm d}n}{{\rm d}M_{\rm h}}{\rm d}M_{\rm h}, \tag{16}$$

the $L_{\rm IR}$–$M_{\rm h}$ relation is derived.

We plot the IR luminosity–halo mass relation at redshift 0.5 and 2 in Fig. 4. For the same reasons given in Section 2.1, we do not consider the IR luminosity dispersion among haloes with the same mass $M_{\rm h}$.

2.3 CO and [C I] emission lines contamination

The CO rotational transition lines from low-redshift galaxies are by far the most important contaminants for the $z > 5$ C II signal. Although some studies aimed at measuring CO LFs exist (e.g. Keres, Yun & Young 2003 and references therein), they lack data either for higher rotational transition numbers, J, or at high redshift. On the other hand, the CO line luminosity is found to be closely related to the IR luminosity, since both lines are good star formation activity tracers (Bayet et al. 2009; Popping et al. 2014).

The CO line luminosity is derived by using the $\log(L_{\rm IR}) = \alpha\log(L_{\rm CO}) + \beta$ relations presented in table 3 of Greve et al. (2014) for lines with J-ladders from 1 to 13. These relations are fitted from samples of local ($z < 0.1$) (U)LIRGs and high-z ($z > 1$) dusty star-forming galaxies (DSFGs). Since CO lines are considered as contaminants to be removed when recovering the [C II] signal, the

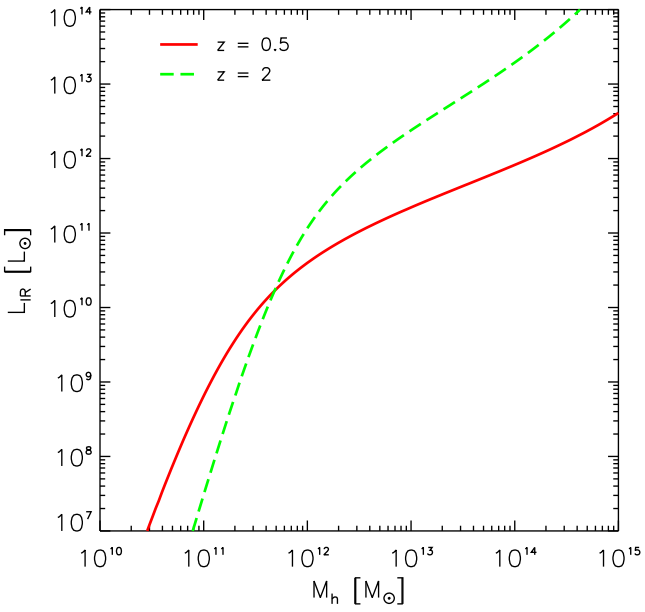

Figure 4. FIR continuum luminosity derived from equation (16) as a function halo mass at redshift $z = 0.5$ and 2.

scatter around the fitting relation should be modelled. To this aim we assume a Gaussian distribution of the form

$$p(L_{\rm CO}|\overline{L}_{\rm CO}) = \frac{1}{\sqrt{2\pi}\sigma}\exp\left[-\frac{x^2}{2\sigma^2}\right], \quad (17)$$

where $x = \log(L_{\rm CO}) - \log(\overline{L}_{\rm CO})$ and $\sigma = s/\alpha$ is the variance; s is the scatter of the data around the $\log(L_{\rm IR}) - \log(\overline{L}_{\rm CO})$ fitting in Greve et al. (2014), including the intrinsic dispersion and statistical errors.

We further consider the contamination from two [C I] fine-structure lines: (i) [C I(1–0)], corresponding to the $^3P_1 \rightarrow {}^3P_0$ transition, at 492 GHz, and (ii) [C I(2–1)], corresponding to the $^3P_2 \rightarrow {}^3P_1$ transition, with frequency 809 GHz. Several authors have reported [C I] observational data (e.g. Gerin & Phillips 2000; Israel & Baas 2002; Walter et al. 2011; Alaghband-Zadeh et al. 2013), finding relations between the [C I] and CO or IR luminosities. Motivated by observations, Popping et al. (2014) have calculated the expected $[{\rm C\,I}]/L_{\rm IR}$ ratios for $0 < z < 2$ galaxies, by combining a semi-analytical galaxy formation model with radiative-transfer and line-tracing calculations. We adopt the outcome of these theoretical calculations and we add 0.25 dex scatters to the mean ratio, namely the maximum of the deviations reported by Popping et al. (2014).

2.4 Instrumental noise

We have to account for instrumental noise, in order to have predictions that can be fairly compared with observation. The noise level of a radio telescope is given by the standard expression

$$\sigma_{\rm N} = \frac{2k_{\rm B}T_{\rm sys}}{A\sqrt{\Delta\nu_0 t}}, \quad (18)$$

where $k_{\rm B}$ is the Boltzmann constant, $T_{\rm sys}$ is the system temperature, A is the area of the antenna, t is the integration time per FOV. If the camera has $N_{\rm pix}$ pixels and the observation is performed at wavelength λ_0, normally the instrument is designed by such a way that $\Omega_{\rm FOV} \sim \lambda_0^2/AN_{\rm pix}$ holds. To cover a sky region of solid angle $\Omega_{\rm map}$, the total integration time is $t_{\rm obs} = t \times \Omega_{\rm map}/\Omega_{\rm FOV}$. We model the instrumental noise as a zero mean Gaussian random variable without spatial and frequency correlation, and we add such fluctuations to the mock maps.

2.5 Mock maps

The light cone for which we produce the intensity maps is built from the halo catalogues of the BolshoiP simulation[4] (Bolshoi simulation with Planck cosmology; see Bolshoi simulation paper Klypin, Trujillo-Gomez & Primack 2011). In the simulation, the smallest haloes resolved are $\approx 5 \times 10^9\,{\rm M}_\odot$, well below the mass of haloes that are expected to host the bulk of [C II] emission (see Sections 2.6).

The box of this simulation is $L = 250\,h^{-1}$ cMpc on a side, corresponding to 2.4 deg when located at $z = 7$. When making light cones from a simulation with a box length smaller than the cone depth, a standard protocol is to replicate the same halo catalogue along the radial direction at the same time applying a 'randomization' procedure made of random translations, rotations, and reflections in order to avoid spurious periodicity effects (Blaizot et al. 2005).

We divide a 2.4×2.4 deg^2 sky region into 200×200 pixels whose angular size is 43 arcsec. This corresponds to the beam size of a 6-m radio telescope for $\lambda_0 = \lambda_{\rm C\,II}(1+7)$. The frequency range [238, 317] GHz ($z_{\rm C\,II} = [7, 5]$) is equally divided into 60 bins with bandwidth of each bin $\Delta\nu_0 = 1.3$ GHz.

Given a pixel in the [C II] map, the measured intensity in the frequency bin centred at ν_0 is

$$I_{\rm C\,II}(\nu_0) = \frac{1}{(\Delta\theta)^2}\sum_j \frac{1}{\Delta\nu_0}\frac{L^j_{\rm C\,II}}{4\pi r_j^2(1+z_j)^2}, \quad (19)$$

where $\Delta\theta$ is the angular size of the pixel and r_j is the comoving distance up to z_j; the sum is performed on all haloes seen by this beam and with redshift

$$\frac{\nu_{\rm C\,II}}{\nu_0 + \Delta\nu_0/2} - 1 \le z_j \le \frac{\nu_{\rm C\,II}}{\nu_0 - \Delta\nu_0/2} - 1. \quad (20)$$

For the CO and [C I] emission lines the procedure is the same as for [C II]. For the FIR continuum, equation (19) becomes

$$I_{\rm FIR}(\nu_0) = \frac{1}{(\Delta\theta)^2}\sum_j \frac{L^j_{\rm IR}{\rm SED}_{\rm IR}(\nu)(1+z_j)}{4\pi r_j^2(1+z_j)^2}, \quad (21)$$

where $\nu = \nu_0(1+z_j)$, and ${\rm SED}_{\rm IR}(\nu)$ is the normalized spectrum template of the galaxy,

$$\int_{c/1000\,\mu{\rm m}}^{c/8\,\mu{\rm m}} {\rm SED}_{\rm IR}(\nu){\rm d}\nu = 1. \quad (22)$$

For simplicity, we choose the Spi4 spiral galaxy SED template from the SWIRE template library[5] (Polletta et al. 2007) as a typical continuum template for all galaxies (note that only the FIR part is used). For all above radiation, we take into account the redshift distortions produced by peculiar motions along the radial direction.

We also generate noise maps at each frequency by adopting[6] $T_{\rm sys} = 150$ K, $N_{\rm pix} = 128 \times 128$, and a total integration time $t_{\rm obs} = 5000$ h. The frequency range that we are considering,

[4] http://www.cosmosim.org/cms/simulations/bolshoip-project/bolshoip/
[5] http://www.iasf-milano.inaf.it/~polletta/templates/swire_templates.html
[6] We consider the third octile of precipitable water vapour, pwv = 0.913 mm, namely the one assumed by the ALMA Sensitivity Calculator (ASC) in the default case. The reader may also refer to fig. 2.14 of the ALMA handbook (https://almascience.eso.org/documents-and-tools/cycle-0/alma-technical-handbook/at_download/file).

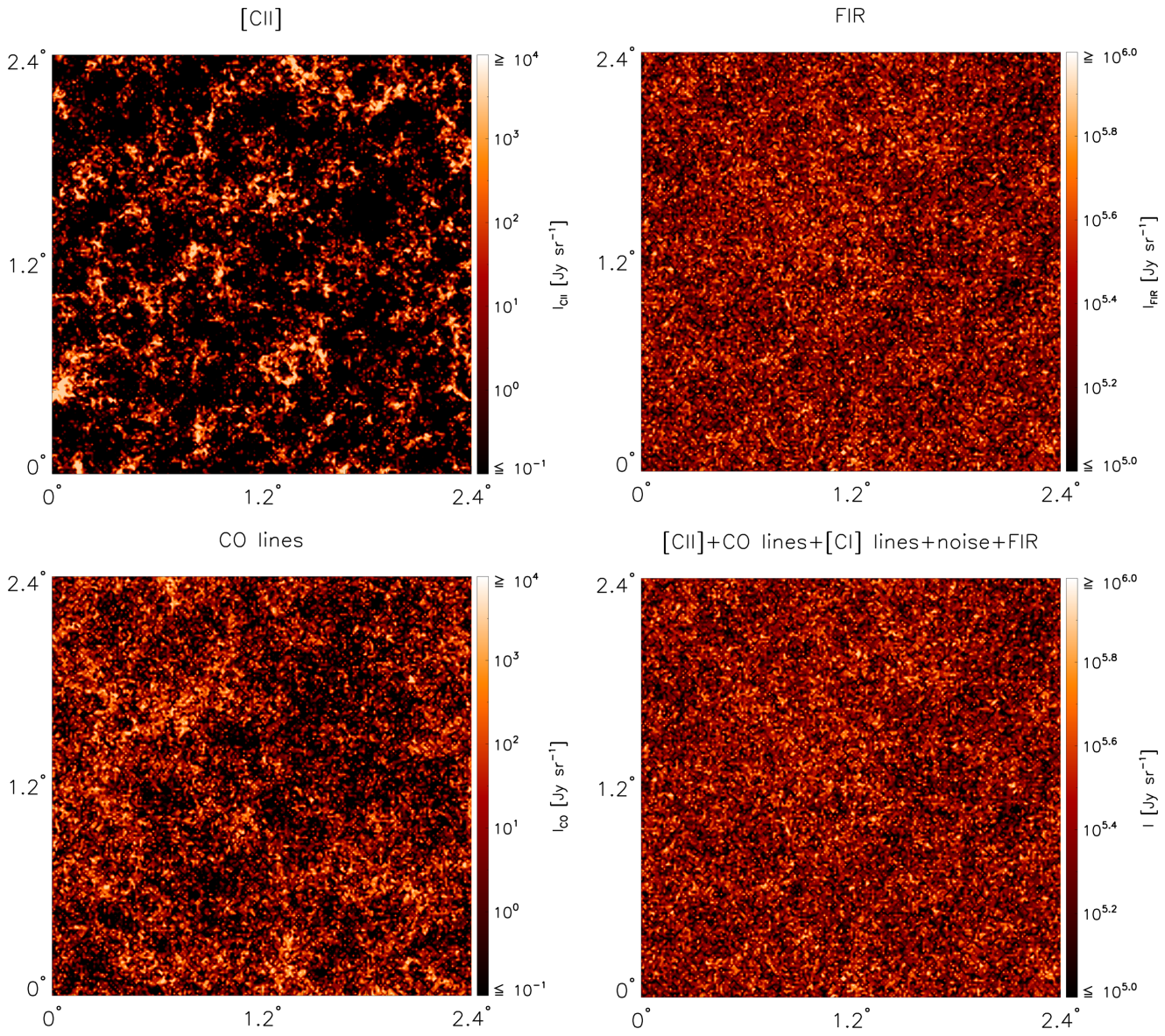

Figure 5. Map of the [C II] signal (top left), FIR continuum foreground (top right), the CO lines contamination (bottom left), and full observed map made by the sum of the signals and instrumental noise (bottom right). All maps are for the (316 ± 0.65) GHz frequency bin. As the emission line signal is much weaker than the continuum, the full map looks very similar to the continuum map.

[238–316] GHz, is sufficiently far from the prominent water atmospheric absorption at 325 GHz. Although there is a deep decreasing trend of transmission with increasing frequency, we note that the transmission is larger than 0.9 at $\nu_0 < 300$ GHz, for pwv = 1 mm, meaning that the [C II] signal from $z > 5.3$ galaxies is not strongly affected by transmission issues. In the case of other atmospheric absorption features, we could simply drop the corresponding frequency bins. This treatment would not strongly affect our conclusions.

For the (316 ± 0.65) GHz frequency bin, maps of [C II] signal, FIR continuum foreground, CO lines contamination and their sum plus the [C I] lines and instrumental noise are shown separately in Fig. 5. The CO map includes all CO lines from $J = 1$ to 13. Fig. 6 shows the mean [C II] signal, FIR continuum, CO lines and [C I] lines as a function of frequency. The FIR continuum is much stronger than the [C II] and contamination emission: for instance, at 316 GHz the FIR continuum is $\sim 3 \times 10^5$ Jy sr^{-1}, while the [C II] signal and the CO contamination are ∼1200 and ∼800 Jy sr^{-1}, respectively. Moreover, although at $z_{\rm C\,II} \sim 5$, the CO lines signal is comparable to the [C II] one, at $z_{\rm C\,II} \sim 7$ CO dominates by a factor ∼20.

At $z_{\rm C\,II} = 5$, the sum of the two [C I] line fluxes is ∼100 Jy sr^{-1}, therefore negligible with respect to the [C II] signal. However at $z_{\rm C\,II} = 7$ it represents an important contamination for [C II] intensity mapping, being ∼60 Jy sr^{-1}, namely comparable to the [C II] signal.

The frequency dependence of the fluctuations of the [C II], FIR, CO, [C I], and the instrumental noise, can be qualitatively appreciated by inspecting a single line of sight cut through the mock light cone, as shown in Fig. 7.

2.6 Recovering the [C II] signal

To recover the [C II] signal from the observed maps it is necessary to subtract the CO and [C I] contamination and FIR

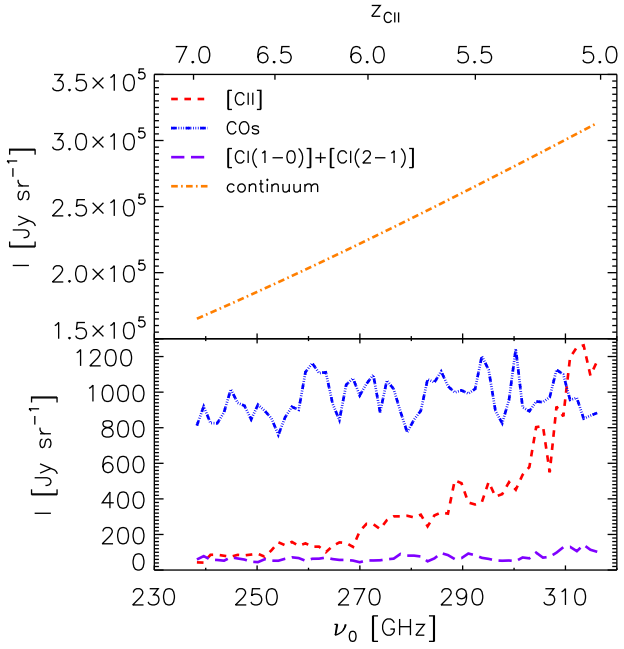

Figure 6. Mean intensity of [C II] signal, CO and [C I] contamination and FIR continuum as a function of observed frequency. The $z_{\rm C\,II}$ is marked on upper abscissa.

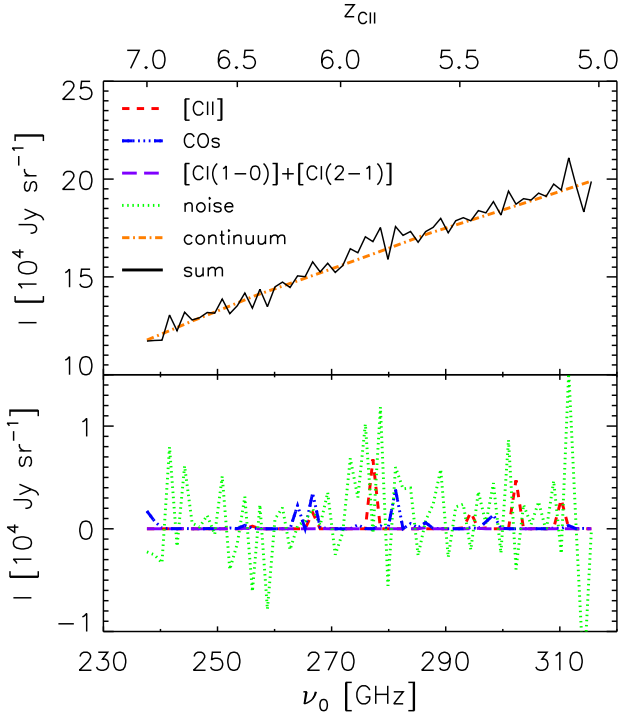

Figure 7. The [C II] signal, CO and [C I] lines contamination, instrumental noise (bottom panel), and the FIR continuum foreground (top panel) as a function of frequency along a randomly selected line of sight cut through the mock light cone.

continuum foreground. For the purpose of contamination subtraction, it is useful to know the fractional contribution from haloes with different mass to the total fluctuations signal coming from galaxy clustering. The clustering term of the angular power spectrum of a line emitted from sources located in a narrow redshift range is

$$P_{\rm clust} \propto \left[\int L(M_{\rm h}) b(M_{\rm h}) \frac{{\rm d}n}{{\rm d}M_{\rm h}} {\rm d}M_{\rm h}\right]^2, \quad (23)$$

where $L(M_{\rm h})$ is the line luminosity and $b(M_{\rm h})$ is the halo bias. For $\nu_0 = 316$ GHz, the observed CO lines with $J = 4$, 5, 6, and 7 are from $z \sim 0.45$, 0.82, 1.18, and 1.54, respectively. Most of the CO contamination to the 316 GHz map is due to these four lines. The two [C I] lines are from $z \sim 0.56$ and 1.56, respectively. Fig. 8 shows the fractional power spectrum from haloes below a certain mass for [C II] and these four CO lines and two [C I] lines. In order to decrease CO and [C I] contamination by >90 per cent, radiation from haloes above $\sim 10^{12}$–3×10^{12} M$_\odot$ must be subtracted. In a 2.4×2.4 deg^2 field there are $\sim 2 \times 10^5$ haloes with $M_{\rm h} > 10^{12}$ M$_\odot$ at all redshifts; however, only those whose CO or [C I] emission lines are received in the frequency bin centred at ν_0 produce contamination.

In principle, decontaminating the map would be easy if we could measure the contamination line flux of each galaxy in the map, then subtract it from the relevant pixels. However, this procedure is very time consuming. Alternatively, we could identify pixels that are supposed to be heavily contaminated by CO or [C I] lines and discard them completely. We note that the CO or [C I] sources should be much brighter than [C II] sources, say, in the optical/IR band, where they are also more easily resolved. Thus, one can directly drop the pixels in which optical/IR bright sources are detected in the redshift range from which CO or [C I] lines are redshifted into the observed frequency bin. Of course, this would also cause a loss of [C II] flux from the dropped pixels. However, as [C II] (CO or [C I]) lines come primarily from high-z (low-z) galaxies, there are no correlations between the two galaxy populations, i.e. removing CO([C I])-bright pixels is equivalent to a random masking of [C II] signal. The missing [C II] power is limited as long as the masking fraction is $\lesssim$30 per cent (Kashlinsky et al. 2005).

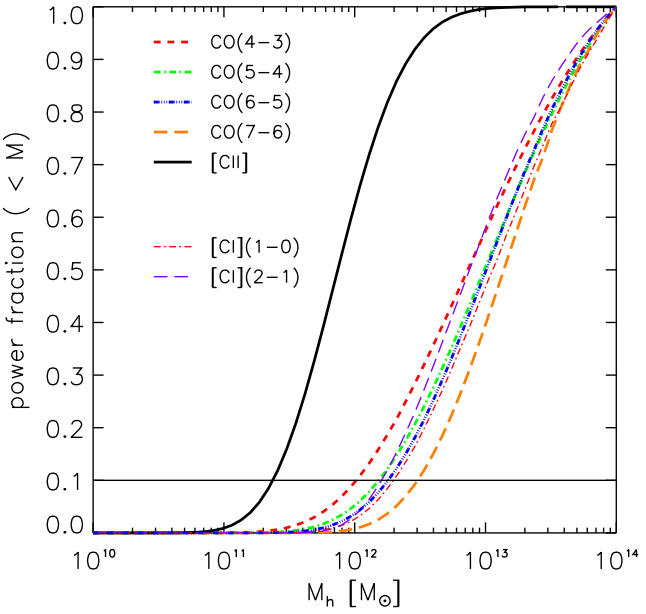

Figure 8. Fractional contribution from haloes below $M_{\rm h}$ to the clustering term (equation 23) of the angular power spectrum for the 316 ± 0.65 GHz frequency bin for various emission lines. The two thin lines refer to [C I(1–0)] and [C I(2–1)] lines, respectively. To guide the eye we have plot a horizontal line corresponding to 0.1.

How do we select optical/IR bright sources? The natural choice is to use the *K*-band magnitude (Silva et al. 2014). However, this quantity may not be a good indicator for IR and CO or [C I] luminosities. For example, the *K* band to total IR flux ratio of the seven spiral galaxy templates in the SWIRE SED library varies by a factor of ∼30. The discrepancy for different galaxy types is even larger. To use the specific *K*-band brightness in contamination removal, the scatter of the L_K–$L_{\rm IR}$ relation should be modelled reasonably.

In the samples used in Greve et al. (2014), we find 51 (U)LIRGs and 15 high-z DSFGs whose *K*-band flux can be found on their web site. From such data, we fit the following $L_{K'}-L_{\rm IR}$ relation:

$$\log\left(\frac{L_{K'}}{\rm erg\,s^{-1}Hz^{-1}}\right) = 0.39\times\log\left(\frac{L_{\rm IR}}{\rm L_\odot}\right)+25.26, \quad (24)$$

with a standard deviation of residuals equal to 0.35; $L_{K'}$ is the luminosity at the rest-frame frequency that is redshifted into *K* band. For a halo with mass $M_{\rm h}$ and IR luminosity $L_{\rm IR}$ (computed from equation 16), $L_{K'}$ is randomly generated from a lognormal distribution with mean given by equation (24) and standard deviation $\sigma_{K'}=0.35$. We find that, for example, a halo with typical IR luminosity $10^{11}\,{\rm L_\odot}$ at $z=1$ is as bright as $m_K=21$ when adopting the Spi4 spiral galaxy SED template. We are then confident that *K*-band luminosities can be safely used to remove CO and [C I] contamination. The advantage with respect to relying on UV/optical magnitudes is that dust extinction effects in the *K* band are much smaller, and can be neglected to a first approximation.

The FIR foreground subtraction algorithm exploits the fact that the continuum is a very smooth function in frequency space. Such feature is widely used, for example, in H I 21-cm intensity mapping (Wang et al. 2006; Jelić et al. 2008; Alonso et al. 2015). For this reason, we believe that assuming the same FIR continuum template for all haloes is acceptable, as smoothness without specifying the slope, is the only feature of the foreground that is required by this algorithm. We check that, adopting a very different SED template, e.g. an elliptical galaxy or a starburst galaxy, results in different slopes and amplitude of predicted FIR foreground, but the recovered [C II] signal is almost identical.

In what follows we list the steps for recovering the [C II] signal from the full, observed map at the 60 frequency bins in which the frequency range [238, 317] GHz ($z_{\rm C\,II}=[7,\,5]$) is sampled ($\Delta\nu_0=1.3$ GHz). They form a set of 200 × 200 line of sights (one for each pixel of the map).

(i) Identify the 'CO or [C I] contaminated' pixels (pixels containing $m_K<22$ galaxies whose contamination lines are redshifted into the relevant band) in each line of sight, replace their flux with the interpolated value from the two neighbouring pixels along the same line of sight.

(ii) For each line of sight, take out its foreground component that is found by either singular value decomposition (SVD), or polynomial fitting algorithm (details are given in Appendix A).

(iii) Set the flux of 'CO or [C I] contaminated' pixels identified in step (i) to be zero.

After the above procedures, the final map contains the [C II] signal, instrumental noise, and relatively negligible FIR continuum foreground and contamination residuals. We check that, at angular scale ∼1000 arcsec, for frequencies corresponding to $z_{\rm C\,II}=5$, 6, and 7, 0.1 per cent, 6 per cent and 20 per cent of the CO contamination power spectrum is left as residuals, respectively. For [C I] lines the corresponding fraction is 2, 5, and 10 per cent, respectively.

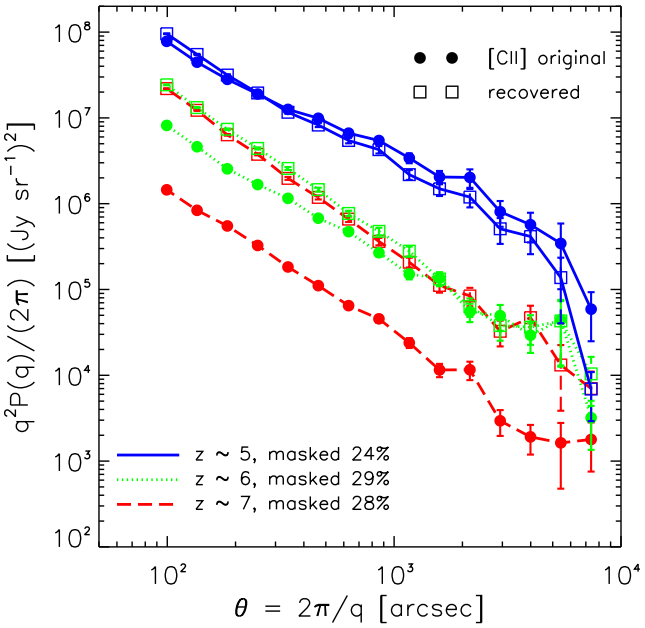

Figure 9. The remaining angular power spectrum after foreground and contamination removal (open squares connected with lines) and the original [C II] signal (filled circles connected with lines) as a function of angular scale $\theta=2\pi/q$, where q is the wavenumber, at $z_{\rm C\,II}\sim5$ (solid), 6 (dotted), and 7 (dashed), respectively. We give the masked percentages for each. The assumed observational configuration is a 6 m telescope with $T_{\rm sys}=150$ K, $N_{\rm pixel}=128\times128$, and a $t_{\rm obs}=5000$ h.

3 RESULTS

Fig. 9 shows the recovered [C II] angular power spectrum (dashed) from $z\sim5$, 6, 7, along with the original signal (solid). At $z_{\rm C\,II}\sim5$, the power spectrum is almost perfectly recovered, with the slight deficiency at large angular scales due to the discarded [C II] flux in CO or [C I] contaminated pixels. At $z_{\rm C\,II}\sim6$, the [C II] signal is recovered for $\theta\gtrsim1000$ arcsec; at smaller scales the limiting factor is the instrumental noise that can however be suppressed by a longer integration time. The signal from $z_{\rm C\,II}\sim7$ remains largely inaccessible, as noise dominates at all scales.

4 CONCLUSIONS AND DISCUSSIONS

We have studied the collective [C II] emission signal from star-forming galaxies at $z\geq5$, as well as the influence of FIR continuum foreground and CO and [C I] contamination on the experimental detection of the signal.

To this aim we have combined the predicted [C II] line luminosity as a function of the galaxy SFR and metallicity (derived from single galaxy simulations including a subgrid treatment of the ISM presented in V15) with a semi-empirical approach to compute the $L_{\rm C\,II}-M_{\rm h}$ relation. This relation is subsequently applied to halo catalogues built from the large-scale *N*-body simulation BolshoiP, to generate mock maps of [C II] signal.

To compute the FIR continuum foreground, we derived the $L_{\rm IR}-M_{\rm h}$ relation via the abundance-matching technique. As for the contamination by CO lines emitted from low-redshift galaxies, instead of using the poorly constrained CO LFs, we use intermediate $L^{\rm J}_{\rm CO}-L_{\rm IR}$ relations that were better fitted from measurements of both local and high-redshift samples. We use the theoretical calculations of the [C I] line luminosities as a function of $L_{\rm IR}$, according to the Popping et al. (2014) model, mentioned in Section 2.5. We

generated mock maps for FIR continuum, CO and [C I] emission, in close analogy with the [C II] mock maps.

We carried out FIR foreground removal and contamination masking experiments on the total mock maps (containing the signal + foreground + contamination and also the instrumental noise) to recover the angular power spectrum of original [C II] maps. We pointed out that, in order to efficiently subtract the CO and [C I] contamination one could discard pixels that are allegedly contaminated by contamination lines. This is feasible if the map has sufficient angular resolution to avoid losing too many pixels. We estimated that if the intensity map has a resolution ∼40 arcsec, contamination can be suppressed by dropping all pixels containing galaxies brighter than $m_K = 22$ and located at the relevant redshift range.

We found that the $z > 5$ [C II] signal comes mainly from haloes in the mass range 10^{11-12} $M_\odot$ (H-band apparent magnitude ∼26.8–23.8); as this mass range is narrow, intensity mapping is an ideal experiment to investigate these early galaxies. The [C II] signal from $z_{C\,II} \sim 5-6$ is detectable for a ground-based, noise-limited telescope with a 6 m aperture, $T_{sys} = 150$ K, an FIR camera with 128 × 128 pixels in about 5000-h total integration time. Although feasible in principle, the experiment is difficult to be performed using currently available telescopes. In addition, the integration time itself could be longer if the atmospheric conditions are on average worse than assumed here. Therefore a dedicated telescope is required and its location is essential. In any case, our study will serve as a robust guideline for the design of future facilities.

A further motivation of a [C II] intensity mapping experiment is to detect the signal from faint galaxies that are unresolved even in deepest optical/IR surveys. This is important as these faint galaxies are believed to contribute most ionizing photons to reionization (Choudhury & Ferrara 2007; Lorenzoni et al. 2011; Salvaterra, Ferrara & Dayal 2011; Bouwens et al. 2012; Finkelstein et al. 2012; Jaacks et al. 2012; Dayal et al. 2013).

In what follows, we therefore discuss the feasibility of such a kind of experiment. As can be seen from Fig. 8, at $z \sim 5$, faint galaxies hosted in haloes below 10^{11} $M_\odot$ only produce less than 1 per cent of the total [C II] power spectrum. Therefore an intensity mapping experiment aimed at detecting such faint galaxies could only be carried out by a telescope whose noise level is background limited, such as a cryogenic space telescope. In this case the noise is mainly due to Poisson fluctuations of the CMB (Visbal & Loeb 2010):

$$\sigma_N = \sqrt{\frac{B(T_{CMB}, \nu_0)h\nu}{\lambda_0^2 \Delta\nu_0 t}}, \quad (25)$$

where B is the CMB emission at ν_0. For the following calculation we adopt a 2-m aperture telescope[7] and $t_{obs} = t \times \Omega_{map}/\Omega_{FOV} = 100$ h, which is appropriate as a reference for a space instrument with a low noise level.

To analyse the [C II] signal of these faint galaxies, the [C II] flux from bright galaxies needs to be measured by a high-resolution interferometer array, and then subtracted in the relevant pixels. In the (316 ± 0.65) GHz frequency bin, in our light cone there are $\sim 7 \times 10^3$ haloes with [C II] line flux $> 10^{-22}$ W m^{-2}. These haloes have $M_h \gtrsim 6 \times 10^{10}$ $M_\odot$. In addition, there are 1.3×10^4 haloes having CO and [C I] contamination line flux above 10^{-22} W m^{-2}. By assuming a line width of 50 km s^{-1}, to resolve these haloes with a signal-to-noise ratio >5, the required sensitivity is 4×10^{-5} Jy. For comparison, at 316 GHz for a channel width of 50 km s^{-1}, ALMA sensitivity with 34 antennas is $\sim 4 \times 10^{-5}$ Jy with 28 h. Assuming an ∼(20 arcsec)^2 FOV for ALMA, to cover a sky region of 2.4 × 2.4 deg^2, we need $\sim 2 \times 10^5$ pointings. Therefore, even for only one frequency bin the required integration time is so high ($\sim 5 \times 10^6$ h!) to make the experiment unfeasible with current technology.

In spite of this, we generate new maps including only the [C II] signal and contamination from haloes with a line flux below $< 10^{-22}$ W m^{-2}. Such haloes have $\lesssim 10^{11}$ $M_\odot$, therefore we can use the $L_{C\,II} - M_h$ relation in P14 simulation. We can recover the [C II] power spectrum using the procedures detailed in Section 2.6, with the following considerations. Here we have assumed that galaxies with [C II]/CO/[C I] line flux above 10^{-22} W m^{-2} have already been resolved. Thus, when removing contamination, we can directly subtract the flux of the resolved sources in the relevant frequency bin, instead of discarding the pixel completely. Additionally, here the [C II] signal to FIR continuum ratio is even smaller, which allows us to take out the first 15 modes in continuum subtraction. In Fig. 10 we show the original and recovered power spectrum from $z_{C\,II} \sim 5$. We can see that the experiment is indeed possible at $z = 5$. At higher redshift, though, the recovery of the [C II] signal from faint galaxies is still hampered by the noise level.

During the final stages of this work, Silva et al. (2014) presented an investigation of the [C II] signal from high-z galaxies through mock surveys obtained from seminumerical simulations. The two studies are in broad agreement, although they differ in the conclusions concerning the FIR continuum, which we found to be much stronger than both the [C II] signal and contamination. Hence, accurately subtracting this foreground is vital in order to recover the [C II] signal. The good news is that we showed here that the proposed algorithm to remove a spectrally smooth component from each line of sight, inspired by 21 cm experiments, can be successfully applied to [C II] intensity mapping as well.

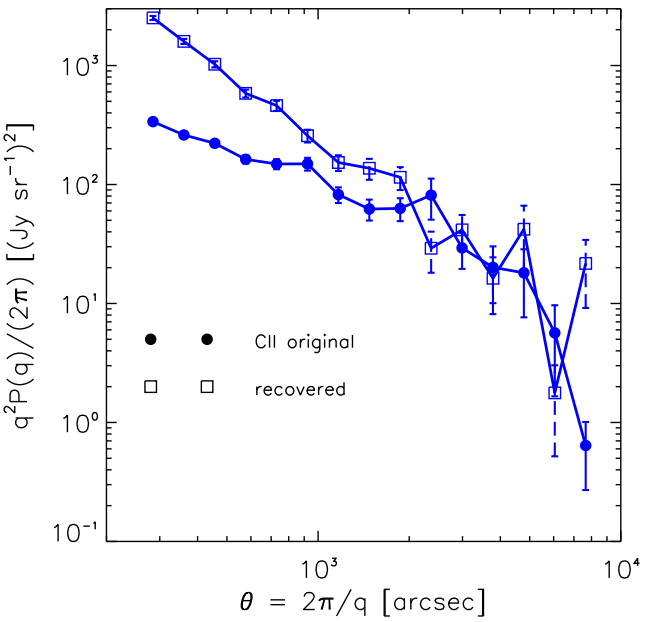

Figure 10. The original angular power spectrum of [C II] emission from haloes with [C II] line flux $< 10^{-22}$ W m^{-2} at the 316 ± 0.65 GHz frequency bin (filled symbols) and the recovered one (open symbols).

[7] A 2-m aperture telescope can be considered typical for a space observatory. While a larger aperture would be more helpful in reducing integration time, the main challenge is to measure the contamination flux of foreground galaxies and [C II] flux of bright high-z galaxies.

Finally, we comment on a possible caveat of our work, related to the fact that the V15 model neglects the contribution of H II regions to the [C II] emission. We have already shown that H II regions in the diffuse medium do not have significant contribution compared with the cold neutral medium and warm neutral medium (see fig. 8 in González-López et al. 2014), and V15 further shows that [C II] emission by cold neutral medium and warm neutral medium is negligible compared with the PDRs. For what concerns H II regions surrounding molecular clouds (MC), we consider the MC properties predicted by the V15 model: number density, $n_{\rm H} \sim 10^3$ cm^{-3}; size, $r_{\rm MC} \sim 1$ pc; ionization parameter[8] $U \sim 10^{-2.7}$. These fiducial values for $n_{\rm H}$ and U are close to the parameters used in fig. 2 of Nagao et al. (2011), where H II regions represent MC outskirts with column density 4×10^{20} cm^{-2}. From this figure, we can see that in correspondence of the MC column density expected by the V15 model ($\sim 3 \times 10^{21}$ cm^{-2}) the [C II] emission is almost 50 times stronger than the one at the edge of the H II regions, implying that the latter only contribute $f_{\rm H\,II} \sim 2$ per cent to the total emission. This calculation allows us to conclude that in the V15 model H II regions are expected to provide a negligible contribution to the total [C II] emission, once compared with PDRs. This conclusion is consistent with the results by Abel (2006). In fact, this author finds that for $n_{\rm H} = 10^3$ cm^{-3} and $U = 10^{-2.7}$, $f_{\rm H\,II} \lesssim 10$ per cent.

The H II regions contribution to the [C II] emission remains, however, a very controversial topic. For example, Oberst et al. (2006, 2011) find $f_{\rm H\,II} \sim (30-40)$ per cent in Carina Nebula, which is a single star formation region in Milky Way. Vasta et al. (2010) report fractions spanning a range 5.5–60 per cent in their samples. Decarli et al. (2014) observed two Lyman Alpha Emitters (LAEs) at $z = 4.7$, concluded that in these LAEs (which are actually members of an interacting system including quasars) most of the [C II] emission is from the ionized medium. However, we also note that Cormier et al. (2015) found that H II regions contribution is typically less than 15 per cent for dwarf galaxies.

To summarize, the contribution of H II regions to the [C II] emission is not clearly known, especially for galaxies at $z > 5$, since [C II] observations are still poor at these epochs. Given that $f_{\rm H\,II}$ is expected to be negligible according to current state-of-the-art theoretical models, we do not consider the [C II] emission from H II regions as a major component in our calculations. Accounting for this contribution (e.g. $f_{\rm H\,II} \sim 30$ per cent) would only enhance the [C II] power spectrum (by a factor of $\sim$2), making the signal stronger.

[8] The quoted value for U is estimated without considering the MC optical depth $\tau_{\rm MC}$ to ionizing photons. If $\tau_{\rm MC}$ is considered, U will become smaller and the [C II] emission from H II regions will further decrease.

REFERENCES

Abel N. P., 2006, MNRAS, 368, 1949
Alaghband-Zadeh S. et al., 2013, MNRAS, 435, 1493
Alonso D., Bull P., Ferreira P. G., Santos M. G., 2015, MNRAS, 447, 400
Bayet E., Gerin M., Phillips T. G., Contursi A., 2009, MNRAS, 399, 264
Béthermin M., Doré O., Lagache G., 2012, A&A, 537, L5
Blaizot J., Wadadekar Y., Guiderdoni B., Colombi S. T., Bertin E., Bouchet F. R., Devriendt J. E. G., Hatton S., 2005, MNRAS, 360, 159
Boselli A., Gavazzi G., Lequeux J., Pierini D., 2002, A&A, 385, 454
Bouwens R. J. et al., 2012, ApJ, 752, L5
Bouwens R. J. et al., 2014, ApJ, 793, 115
Bouwens R. J. et al., 2015, ApJ, 803, 34
Breysse P. C., Kovetz E. D., Kamionkowski M., 2014, MNRAS, 443, 3506
Choudhury T. R., Ferrara A., 2007, MNRAS, 380, L6
Cicone C. et al., 2015, A&A, 574, A14
Cormier D. et al., 2015, preprint (arXiv:1502.03131)
Cox P. et al., 2011, ApJ, 740, 63
Dayal P., Dunlop J. S., Maio U., Ciardi B., 2013, MNRAS, 434, 1486
De Breuck C., Maiolino R., Caselli P., Coppin K., Hailey-Dunsheath S., Nagao T., 2011, A&A, 530, L8
De Breuck C. et al., 2014, A&A, 565, A59
de Looze I., Baes M., Bendo G. J., Cortese L., Fritz J., 2011, MNRAS, 416, 2712
De Looze I. et al., 2014, A&A, 568, A62
Decarli R. et al., 2014, ApJ, 782, L17
Duncan K. et al., 2014, MNRAS, 444, 2960
Finkelstein S. L. et al., 2012, ApJ, 758, 93
Gallerani S. et al., 2012, A&A, 543, A114
Gerin M., Phillips T. G., 2000, ApJ, 537, 644
Gong Y., Cooray A., Silva M. B., Santos M. G., Lubin P., 2011, ApJ, 728, L46
Gong Y., Cooray A., Silva M., Santos M. G., Bock J., Bradford C. M., Zemcov M., 2012, ApJ, 745, 49
Gong Y., Cooray A., Santos M. G., 2013, ApJ, 768, 130
González-López J. et al., 2014, ApJ, 784, 99
Greve T. R. et al., 2014, ApJ, 794, 142
Gruppioni C. et al., 2013, MNRAS, 432, 23
Herrera-Camus R. et al., 2015, ApJ, 800, 1
Israel F. P., Baas F., 2002, A&A, 383, 82
Jaacks J., Choi J.-H., Nagamine K., Thompson R., Varghese S., 2012, MNRAS, 420, 1606
Jelić V. et al., 2008, MNRAS, 389, 1319
Kashlinsky A., Arendt R. G., Mather J., Moseley S. H., 2005, Nature, 438, 45
Kennicutt R. C., Jr, 1998, ARA&A, 36, 189
Keres D., Yun M. S., Young J. S., 2003, ApJ, 582, 659
Klypin A. A., Trujillo-Gomez S., Primack J., 2011, ApJ, 740, 102
Leitherer C. et al., 1999, ApJS, 123, 3
Leitherer C., Ortiz Otálvaro P. A., Bresolin F., Kudritzki R.-P., Lo Faro B., Pauldrach A. W. A., Pettini M., Rix S. A., 2010, ApJS, 189, 309
Lidz A., Furlanetto S. R., Oh S. P., Aguirre J., Chang T.-C., Doré O., Pritchard J. R., 2011, ApJ, 741, 70
Lorenzoni S., Bunker A. J., Wilkins S. M., Stanway E. R., Jarvis M. J., Caruana J., 2011, MNRAS, 414, 1455
Magnelli B., Elbaz D., Chary R. R., Dickinson M., Le Borgne D., Frayer D. T., Willmer C. N. A., 2009, A&A, 496, 57
Magnelli B. et al., 2013, A&A, 553, A132
Maiolino R. et al., 2005, A&A, 440, L51
Maiolino R., Caselli P., Nagao T., Walmsley M., De Breuck C., Meneghetti M., 2009, A&A, 500, L1
Mannucci F., Cresci G., Maiolino R., Marconi A., Gnerucci A., 2010, MNRAS, 408, 2115
Meurer G. R., Heckman T. M., Calzetti D., 1999, ApJ, 521, 64
Nagao T., Maiolino R., Marconi A., Matsuhara H., 2011, A&A, 526, A149
Oberst T. E. et al., 2006, ApJ, 652, L125
Oberst T. E., Parshley S. C., Nikola T., Stacey G. J., Löhr A., Lane A. P., Stark A. A., Kamenetzky J., 2011, ApJ, 739, 100
Ota K. et al., 2014, ApJ, 792, 34
Ouchi M. et al., 2013, ApJ, 778, 102
Pallottini A., Ferrara A., Gallerani S., Salvadori S., D'Odorico V., 2014, MNRAS, 440, 2498 (P14)
Polletta M. et al., 2007, ApJ, 663, 81
Popping G., Pérez-Beaupuits J. P., Spaans M., Trager S. C., Somerville R. S., 2014, MNRAS, 444, 1301
Pullen A. R., Doré O., Bock J., 2014, ApJ, 786, 111
Salvaterra R., Ferrara A., Dayal P., 2011, MNRAS, 414, 847
Schaerer D., Boone F., Zamojski M., Staguhn J., Dessauges-Zavadsky M., Finkelstein S., Combes F., 2015, A&A, 574, A19
Schechter P., 1976, ApJ, 203, 297
Sheth R. K., Tormen G., 1999, MNRAS, 308, 119
Sheth R. K., Mo H. J., Tormen G., 2001, MNRAS, 323, 1

Silva M. B., Santos M. G., Gong Y., Cooray A., Bock J., 2013, ApJ, 763, 132
Silva M. B., santos M. G., Cooray A., Gong Y., 2014, preprint (arXiv:1410.4808)
Uzgil B. D., Aguirre J. E., Bradford C. M., Lidz A., 2014, ApJ, 793, 116
Vallini L., Gallerani S., Ferrara A., Baek S., 2013, MNRAS, 433, 1567
Vallini L., Gallerani S., Ferrara A., Pallottini A., Yue B., 2015, submitted (V15)
Vasta M., Barlow M. J., Viti S., Yates J. A., Bell T. A., 2010, MNRAS, 404, 1910
Vázquez G. A., Leitherer C., 2005, ApJ, 621, 695
Venemans B. P. et al., 2012, ApJ, 751, L25
Visbal E., Loeb A., 2010, J. Cosmol. Astropart. Phys., 11, 16
Visbal E., Trac H., Loeb A., 2011, J. Cosmol. Astropart. Phys., 8, 10
Walter F., Weiß A., Downes D., Decarli R., Henkel C., 2011, ApJ, 730, 18
Wang X., Tegmark M., Santos M. G., Knox L., 2006, ApJ, 650, 529
Wang R. et al., 2013, ApJ, 773, 44
Willott C. J., Omont A., Bergeron J., 2013, ApJ, 770, 13

APPENDIX A: FOREGROUND SUBTRACTION

Each line of sight is a 60-elements vector $\boldsymbol{A}_i$ where the smooth FIR continuum is the dominant component. Thus, to subtract the FIR continuum it is necessary first to find its principle components, and then to subtract them from $\boldsymbol{A}_i$. In other words, expressing $\boldsymbol{A}_i$ as the linear combination of a series of base vectors that are orthogonal to each other, i.e $\boldsymbol{A}_i = \sum_j b_j \boldsymbol{B}_j$; b_j indicates the contribution of each vector to the $\boldsymbol{A}_i$. With descending order of b_j, the summary of the first several $\boldsymbol{B}_j$ is considered as the FIR component. To find the principle components, the 60 × 60-elements covariance matrix is

$$\mathbf{C} = \frac{1}{N}\sum_{i}^{N} \boldsymbol{A}_i \otimes \boldsymbol{A}_i,$$

where $N = 200 \times 200$ is the number of line of sights. By performing SVD on this matrix a series of eigenvectors sorted in descending eigenvalues S_j are obtained; they are $\boldsymbol{B}_j$. Then b_j is obtained as $b_j = \boldsymbol{A}_i \cdot \boldsymbol{B}_j$. S_j descends more gently after a certain $j_{\max}$ ($j_{\max} = 2$ for recovering our Fig. 9, and $j_{\max} = 15$ for recovering our Fig. 10), therefore most FIR continuum is considered to be represented by the first $j_{\max}$ principle components.

In the frequency range considered in this work, the FIR continuum is very close to a power law, thus we try the polynomial fitting algorithm as well. The FIR continuum is found to be well fitted by polynomial up to two orders and the recovered [C II] angular spectrum is quite similar. In the main text, we have presented results obtained by adopting the SVD method. However, the polynomial fitting method would have provided consistent results.

This paper has been typeset from a TEX/LATEX file prepared by the author.